RSC Advances

PAPER

View Article Online
View Journal | View Issue

Cite this: *RSC Adv.*, 2019, **9**, 32510

Transition metal oxide@hydroxide assemblies as electrode materials for asymmetric hybrid capacitors with excellent cycling stabilities

Pengfei Hu,[a] Ying Liu,[a] Jianrong Song,[a] Xiufeng Song[b] and Xiang Wu *[a]

Received 20th August 2019
Accepted 28th September 2019

DOI: 10.1039/c9ra06514h

rsc.li/rsc-advances

In this work, three-dimensional cactus-like Co_3O_4@$Ni(OH)_2$ electrode materials are grown directly on Ni foam *via* a two-step hydrothermal method. The as-prepared products possess a specific capacitance of 464.5 C g^{-1} at 0.5 A g^{-1} and 91.67% capacitance retention after 20 000 cycles. The as-assembled device using the as-synthesized samples as positive electrodes delivers an energy density of 112.5 W h kg^{-1} at a power density of 1350 W h kg^{-1}. The superior electrochemical performance of the electrode materials can be attributed to their unique structure, the synergistic effect between Co_3O_4 and $Ni(OH)_2$ materials and reversible reaction kinetics. It suggests that the products are potential alternatives in future energy storage devices.

1. Introduction

With the increasing depletion of fossil fuels and serious environmental pollution, to develop and design clean, renewable energy sources and emerging energy storage devices is a very imperious task.[1–4] Among them, supercapacitors have attracted increasing attention due to their fast charging-discharging, high power density, long cycle life and environmental friendly characteristics.[5–8] Carbon materials and conductive polymers with high specific surface area and low internal resistance have been widely investigated. For example, Fang and co-workers reported hierarchical porous carbon nanorods with a capacitance of 274 F g^{-1} at 0.5 A g^{-1}.[9] Liu *et al.* prepared MoS_2/Ni_3S_2@PPy samples showing a specific capacitance of 845 C g^{-1} at 1 A g^{-1}.[10] However, poor cycling stability hinders their further application. Therefore, it is urgent to develop novel electrode materials with the desired architectures and properties.

As electrode materials, transition metal oxides and hydroxides possess large theoretical capacity and accessible active sites for redox reaction.[11–21] Therein Co_3O_4 materials possess a theoretical capacitance of 3500 F g^{-1} and tailoring spatial structures.[22,23] Many research groups have reported Co_3O_4 structures as electrode materials with various shapes and structures for capacitors. For instance, Zhang *et al. in situ* synthesized Co_3O_4 samples by a facile hydrothermal reaction with a capacitance of 621.8 F g^{-1} at 1 A g^{-1}.[24] Chen and co-worker reported Co_3O_4 nanorod arrays by chemical bath deposition showing a capacitance of 387.25 F g^{-1} at 1 A g^{-1}.[25] Gao *et al.* prepared Co_3O_4 nanowires using a template-free process and obtained a capacitance of 746 F g^{-1} at 1 A g^{-1}.[26] Nevertheless, the practical capacity is far lower than their theoretical one, which limits their future applications in energy storage fields.[27,28] Thus, to construct hybrid electrode materials with unique spatial architectures and high capacity is very important.

Two dimensional layered $Ni(OH)_2$ nanostructures enable fast diffusion of electrons, which make active sites for redox reaction easily accessible.[29–31] For example, Yang's group reported $Ni(OH)_2$ electrode exhibiting a specific capacitance of 2110 F g^{-1} at 1 A g^{-1}.[32] Xiong *et al.* synthesized $Ni(OH)_2$ nanosheets with a capacitance of 2384.3 F g^{-1} at 1 A g^{-1}.[33] Dai *et al.* prepared $Ni(OH)_2$ nanocrystals grown on graphene sheets showing a capacitance of 1335 F g^{-1} at 1 A g^{-1}.[34] Herein, we design a kind of cactus-like Co_3O_4@$Ni(OH)_2$ structure on Ni foam through a facile two-step hydrothermal approach. The as-prepared products show a specific capacitance of 464.5 C g^{-1} at 0.5 A g^{-1} and 91.67% of capacitance retention after 20 000 cycles. A capacitor is assembled using Co_3O_4@$Ni(OH)_2$ as positive electrode and active carbon as negative electrode, respectively. It delivers an energy density of 112.5 W h kg^{-1} at power density of 1350 W kg^{-1}. The excellent performance could be attributed to fast ion transport channel, which constructed by direct contact between two materials and synergistic effect.

2. Experimental

All the chemicals in this work are of analytical grade and directly used without further purification. Ni foam was treated, which is similar to our previous report.[35] In a typical procedure, 3 mmol $Co(NO_3)_2 \cdot 6H_2O$ (0.8731 g), 4 mmol NH_4F (0.1482 g) and 10 mmol $CO(NH_2)_2$ (0.6006 g) were dissolved in 50 mL deionized water and stirred to form a homogeneous solution. Then

[a]*School of Materials Science and Engineering, Shenyang University of Technology, Shenyang 110870, P. R. China. E-mail: wuxiang05@163.com; wuxiang05@sut.edu.cn*
[b]*School of Materials Science and Engineering, Nanjing University of Science and Technology, Nanjing, P. R. China*

the above solution was transferred into a 100 mL autoclave and a piece of pretreated Ni foam was immersed into it. The autoclave was sealed and heated at 120 °C for 6 h. After cooling down to room temperature naturally, the Ni foam was taken out and washed with ethanol and deionized water for three times, respectively, to remove possible impurities or excess ions. After that, it was dried at 60 °C for 12 h. Subsequently, the as-prepared samples were obtained by annealing at 350 °C for 2 h. The average mass loading is 2.1 mg cm^{-2}. Then Ni foam coated Co_3O_4 nanowires were immersed into solution of $Ni(NO_3)_2$ and transferred to same volume of autoclave at 120 °C for 8 h. After cooled to room temperature, the as-prepared samples were cleaned and then dried at 60 °C for 12 h. The mass loading is 4.8 mg cm^{-2}.

The morphology and crystal structure of as-prepared products were analyzed using an X-ray diffraction analyzer (XRD, Shimadzu 7000, Cu Kα radiation, λ = 0.15406 nm, 40 kV), scanning electron microscope (SEM; Gemini SEM 300-71-31). Element compositions were studied by element mappings. The chemical states of products were recorded by X-ray photoelectron (ESCALAB 250).

Electrochemical performances of the as-synthesized products were investigated on a workstation (Shanghai Chenhua, CHI660E) in a three-electrode system. The samples were used as working electrode, Hg/HgO as reference one and Pt foil as counter one. Cyclic voltammetry (CV), galvanostatic charge-discharge (GCD) and electrochemical impedance spectroscopy (EIS) measurements were conducted in 3 M KOH aqueous electrolyte. Specific capacitance (C_s) was obtained from GCD curves according to following equation:

$$C_s = I\Delta t/m \quad (1)$$

where I (A) is discharge current, Δt (s) refers to discharge time, and m (g) represents the mass loading of electrode.

Activated carbon, super p and polyvinylidene difluoride (PVDF) with a mass ratio of 7 : 2 : 1 were mixed on Ni foam as negative electrode for supercapacitor. Quasi-solid-state polyvinyl alcohol (PVA)-KOH electrolyte was made by mixing 2 g PVA and 2 g KOH in 20 mL deionized water. The mass loading of active carbon was calculated based on charge balance theory ($Q^+ = Q^-$), where Q^+ and Q^- represents stored charges that can be calculated as follow:

$$Q = C_s \times \Delta V \times m \quad (2)$$

where C_s is specific capacitance (C g^{-1}), ΔV refers voltage window, m names the mass loading of active materials (g). The mass ratio of active materials can be obtained by following equation:

$$m^+/m^- = C_s^- \times \Delta V^-/C_s^+ \times \Delta V^+ \quad (3)$$

The optimal mass ratio of Co_3O_4@$Ni(OH)_2$//AC is 0.45. Energy density E (W h kg^{-1}) and power density P (W kg^{-1}) of the device can be calculated from the equations:

$$E = 1/2 \times C_s \times \Delta V^2 \quad (4)$$

$$P = E \times 3600/\Delta t \quad (5)$$

where ΔV (V) is voltage window of device, Δt (s) is discharge time.

3. Results and discussion

The phase purity and crystal structure of products are firstly characterized by XRD, as shown in Fig. 1a. All diffraction peaks (black line) of samples located at 19.0° (111), 31.2° (220), 36.8° (311), 38.5° (222), 55.6° (422), 59.3° (511) and 65.2° (440) can be indexed to Co_3O_4 (JCPDS No.42-1467). The diffraction peaks (red line) at 19.2°, 33.1°, 39.1°, 59.1° and 62.7° correspond to (001), (100), (002), (110), (111) crystal planes, which can be assigned to $Ni(OH)_2$ (JCPDS No.14-0117). From the diffraction peaks (blue line), Co_3O_4@$Ni(OH)_2$ products are successful prepared.

XPS is used to further study elemental composition and chemical states of products. The survey spectra (Fig. 1b) show the presence of Co, Ni and O elements. C is from the base. The de-convolution of Ni 2p XPS spectra in Fig. 1c presents two characteristic peaks of Ni $2p_{3/2}$ and Ni $2p_{1/2}$ at 855.5 and 873.1 eV and two satellite peaks at 862 and 879 eV, respectively.[36] Fig. 1d indicates that Co 2p spectra consist of Co^{2+} and Co^{3+}. It could be de-convoluted into two sharp peaks and two satellite peaks. The peaks at 779.3 and 794.5 eV are related to Co^{3+} and those at 781 and 796.2 eV might be ascribed to Co^{2+}.[37] The peaks of O 1s spectra (Fig. 1e) at 529.7, 531.2 and 532.5 eV are associated with metal–oxygen bond, hydroxyl (OH^-) and surface absorbed water, respectively.[38] Elemental distributions of products are also investigated by element mappings, demonstrating that elements are uniformly distributed on the Ni foam, as shown in Fig. 1f.

Fig. 2a is SEM images of as-prepared Co_3O_4 products. It shows that they consist of many nanowires. Further observation (Fig. 2d) finds that the average diameter of the nanowires is 70 nm. Fig. 2b shows SEM images of $Ni(OH)_2$ sample, revealing that dense sheet-like structures appear. Local images can be seen in Fig. 2e. From SEM images shown in Fig. 2(c and f), it is found that hybrid materials consist of many nanowires and nanosheets that interconnect with each other to form unique three-dimensional cactus-like structures.

Electrochemical performances of as-synthesized products are studied in 3 M KOH aqueous solution in a three-electrode system. Fig. 3a–c show CV curves of three electrodes at scan rate from 5 to 50 mV s^{-1}. CV curves of composite electrode present a pair of redox peaks, revealing that capacitive behavior of electrode materials. The redox peaks correspond to faradaic redox reactions during charging-discharging process as follows:[39,40]

$$Co_3O_4 + OH^- + H_2O \leftrightarrow 3CoOOH + e^- \quad (6)$$

$$CoOOH + OH^- \leftrightarrow CoO_2 + H_2O + e^- \quad (7)$$

$$Ni(OH)_2 + OH^- \leftrightarrow NiOOH + H_2O + e^- \quad (8)$$

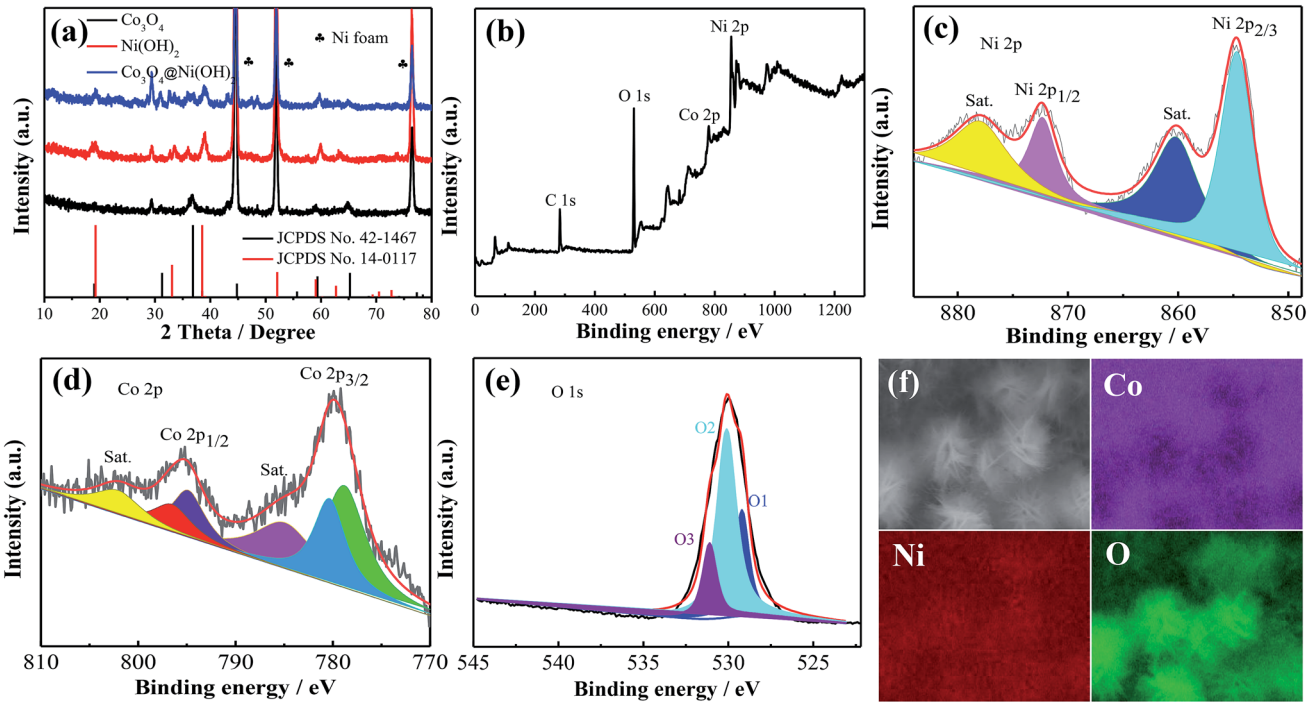

Fig. 1 (a) XRD patterns of the products and XPS spectra of Co_3O_4@$Ni(OH)_2$ sample (b) survey spectra (c) Ni 2p (d) Co 2p (e) O 1s (f) EDS of the composites.

The shapes of CV curves maintains well, indicating excellent reversibility of redox reaction. The corresponding GCD curves of samples are shown in Fig. 3d–f. According to GCD curves of hybrid electrodes at various current densities, specific capacitances are 464.5, 407, 322, 240, and 180 C g^{-1} at 0.5, 1, 2, 4 and 6 A g^{-1}, respectively.

Fig. 4a shows CV curves of as-synthesized products and pure Ni foam at 20 mV s^{-1}. Obviously, the effect of pure Ni foam on capacities of the samples can be neglected due to its insignificant contribution. It is accordance with previous reports.[41] The integrated area of CV curve of Co_3O_4@$Ni(OH)_2$ samples is relatively larger, suggesting that composite electrode possesses a high capacitance. Fig. 4b shows GCD curves of three electrode

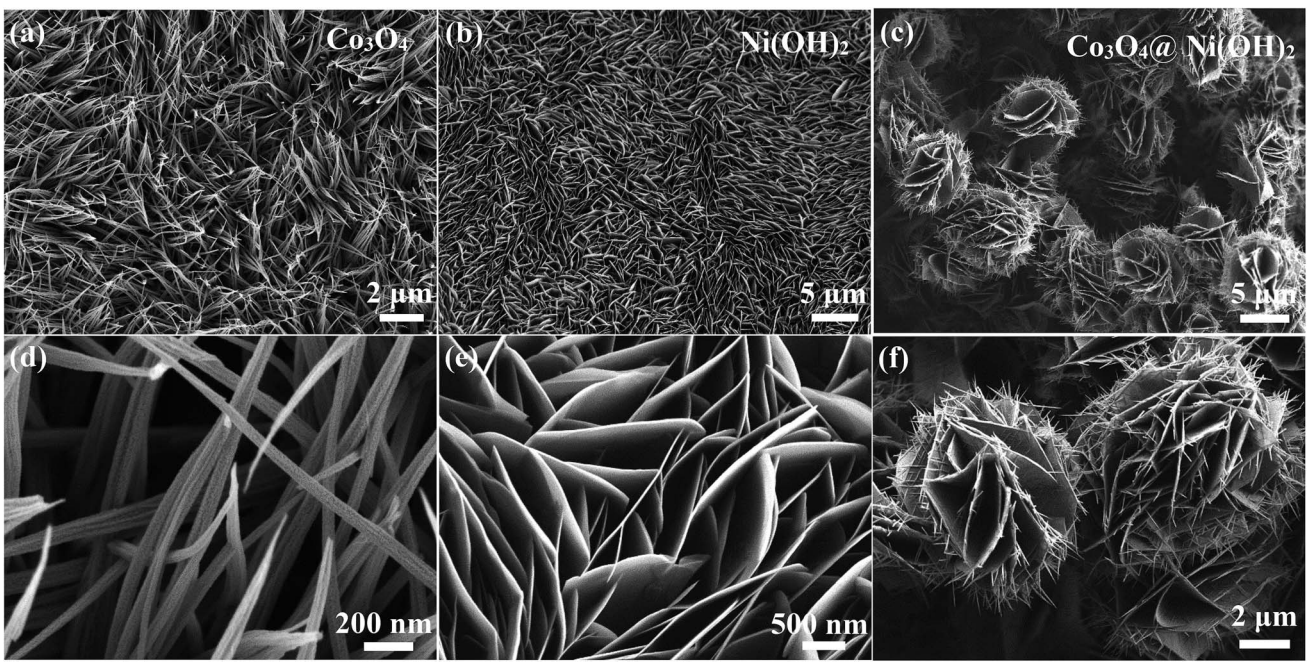

Fig. 2 SEM images of the samples (a and d) Co_3O_4 (b and e) $Ni(OH)_2$ (c and f) Co_3O_4@$Ni(OH)_2$.

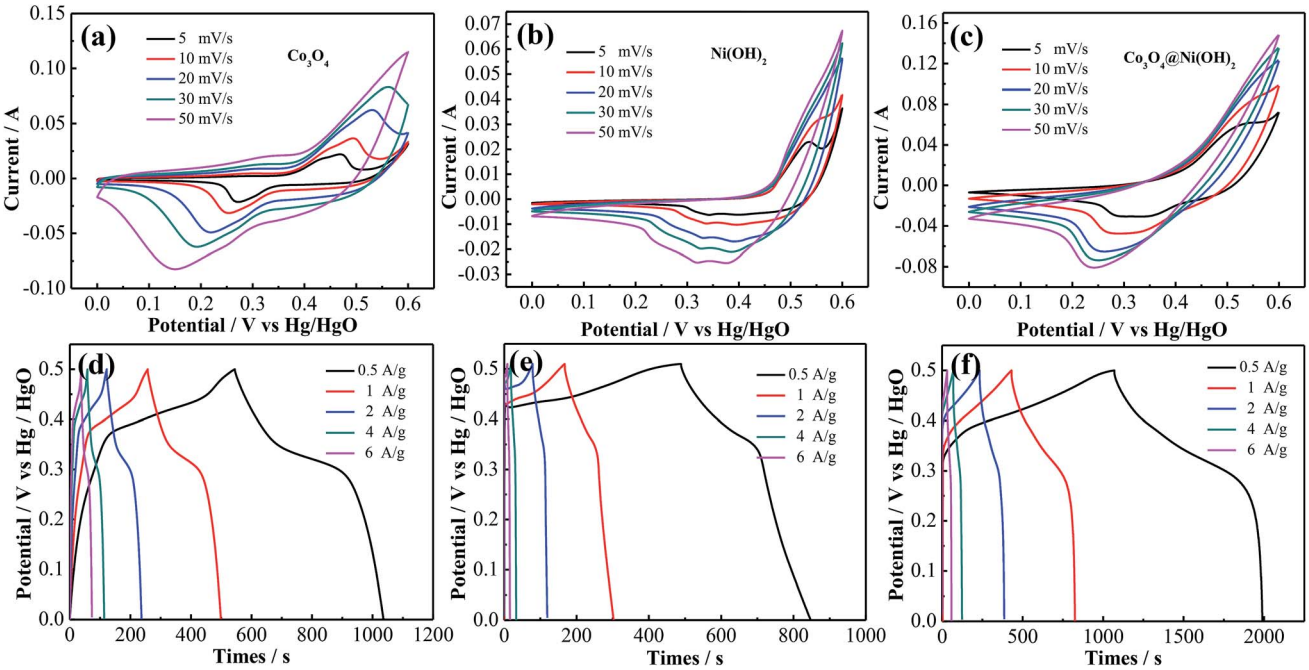

Fig. 3 Electrochemical performance of three electrodes (a–c) CV curves (d–f) GCD curves.

materials at the same current density. The discharge time of hybrid electrode is longer than two other samples.

To further investigate the conductivity of as-synthesized products, EIS are conducted within frequency range from 0.01 to 10^5 Hz. Fig. 4c demonstrates Nyquist plots of all samples, which include a semicircle at high frequency region and a straight line at low frequency one. The former represents equivalent series resistance (E_{SR}), the latter corresponds to Warburg resistance. E_{SR} of Co_3O_4@$Ni(OH)_2$, Co_3O_4, $Ni(OH)_2$ are 0.74, 0.88, 1.45 ohm cm^{-2}, respectively, suggesting that hybrid electrode possesses a low internal resistance.

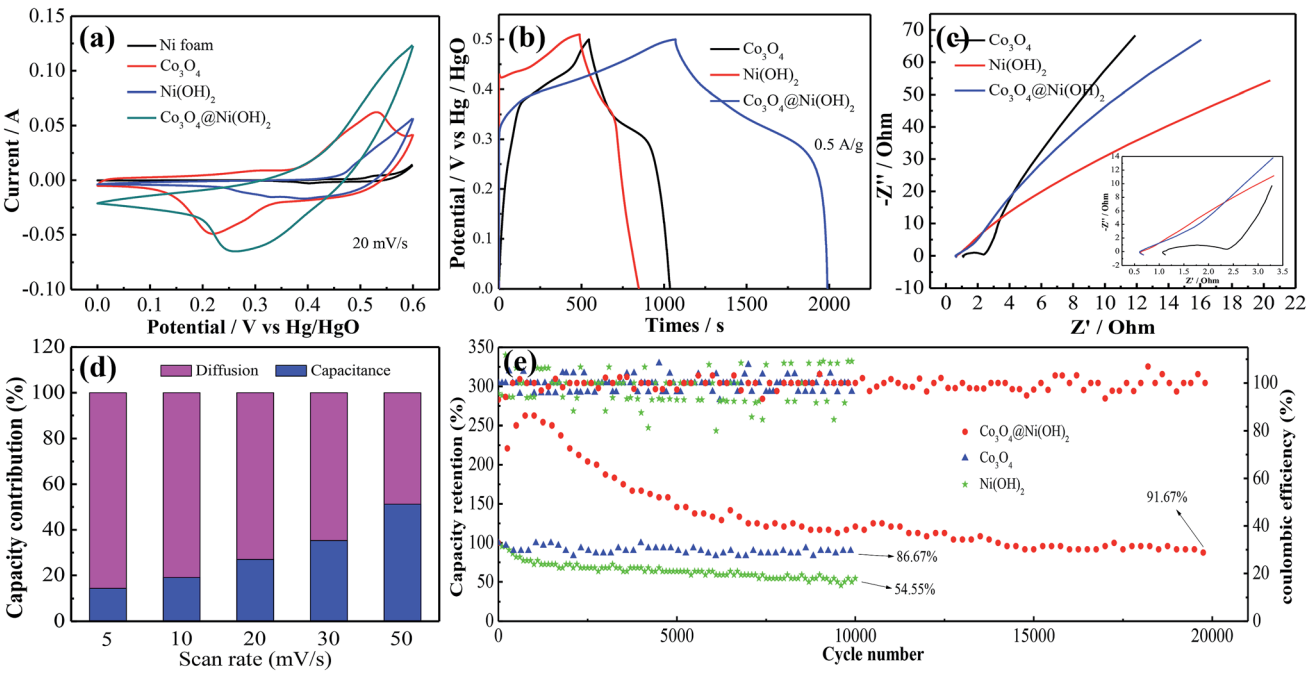

Fig. 4 Electrochemical performance of the electrodes (a) CV curves (b) GCD curves (c) Nyquist plots (d) contribution ratio between diffusion and capacitance (e) cycling performance.

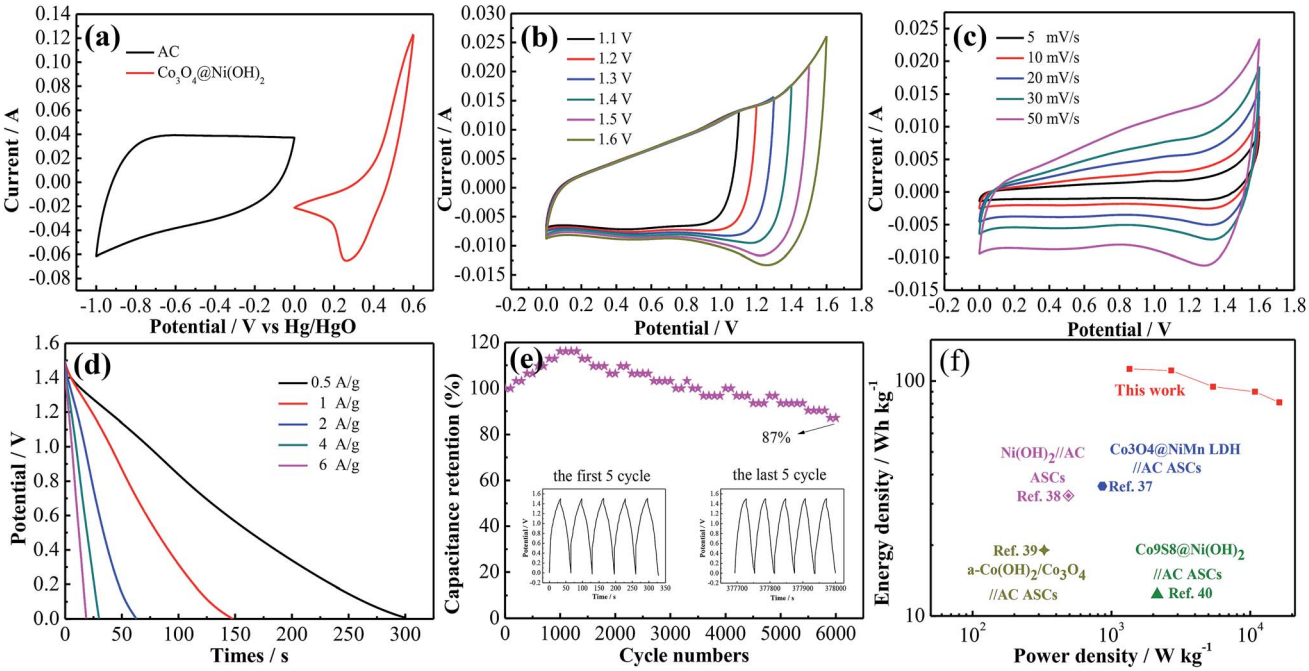

Fig. 5 (a) CV curves of Co_3O_4@$Ni(OH)_2$ and AC electrode at 20 mV s^{-1} (b and c) CV curves of device (d) GCD curves (e) cycling performance (f) Ragone plot.

To understand surface and diffusion behavior of electrodes, the normalization formulas for CV kinetics analysis are listed as follows:[42]

$$i = av^b \quad (9)$$

$$i/v^{1/2} = av^{1/2} + b \quad (10)$$

where a and b are constants, i and v represent current and scan rate, respectively. As shown in Fig. 4d, diffusion controlled contribution is dominant, revealing that battery-type behavior of electrode materials. Cycling stabilities (Fig. 4e) of as-synthesized samples are investigated at 6 A g^{-1}. It can be seen that the capacitance retention ratio of hybrid electrode can reach 91.67% after 20 000 cycles, which is much higher than other two ones. The excellent cycling stability might benefit from synergistic effect between two electrodes. The activation of electrode materials results in the increases of specific capacitance in the initial cycles. With the adding of cycle times, electrode materials are gradually infiltrated by electrolyte, which results in an increase in capacitance.

To estimate its practical application, a hybrid capacitor is assembled using as-prepared products and active carbon as positive and negative electrodes, respectively. CV curves of two electrodes show stable voltage windows between 0 and 0.6 V and between −1 and 0 V, respectively (Fig. 5a). The curves at 50 mV s^{-1} indicate that the device can work at 1.6 V, as shown in Fig. 5b. CV curves of device at scan rates from 5 to 50 mV s^{-1} (Fig. 5c) exhibits that it possesses ideal capacitive performance. According to GCD curves at various current densities (Fig. 5d), the device delivers a capacitance of 150 C g^{-1} at 0.5 A g^{-1}. It keeps 87% of initial capacitance after 6000 cycles in Fig. 5e.

Energy density and power density of device are two significant parameters in actual applications. Fig. 5f shows Ragone plots of some devices. The device presents an energy density of 112.5 W h kg^{-1} at power density of 1350 W kg^{-1}, which are better than some previous reports.[40,43–45] According to Table 1, the hybrid electrode materials reported here possess high specific capacitance and excellent cycling stability.[23,46–49]

Table 1 Electrochemical performance comparison of various electrode materials

Materials	Specific capacitance (1 A g^{-1})	Electrolyte	Retention rate	Ref.
Co_3O_4 mesoporous nanoneedle	668 F g^{-1} (367.4 C g^{-1})	2 M KOH	104% (10 000 cycles)	23
α-$Co(OH)_2/Co_3O_4$ flakes	583 F g^{-1} (291.5 C g^{-1})	2 M KOH	87.6% (1000 cycles)	46
Sandwich-like Co_3O_4/CNTs	562 F g^{-1} (252.9 C g^{-1})	3 M KOH	96% (5000 cycles)	47
2D $MoSe_2$–$Ni(OH)_2$ nanohybrid	933 F g^{-1} (419 C g^{-1})	6 M KOH	91.6% (5000 cycles)	48
Co_3O_4 nanosheets	581 F g^{-1} (261.4 C g^{-1})	2 M KOH	91% (5000 cycles)	49
Co_3O_4@$Ni(OH)_2$ cactus	407 C g^{-1}	3 M KOH	91.67% (20 000 cycles)	This work

4. Conclusion

In summary, we have fabricated a kind of cactus-like 3D Co_3O_4@$Ni(OH)_2$ structure on Ni foam *via* two-step hydrothermal process. Benefiting from the unique architecture, the as-obtained products possess superior electrochemical performances due to the synergistic effects between two single materials. Moreover, the device presents high energy density and excellent cycling stability. It demonstrates that the hybrid architectures can be used as alternative electrode materials in high-performance energy storage devices.

Conflicts of interest

There are no conflicts to declare.

Acknowledgements

This project is supported by the Fundamental Research Funds for the Central Universities (No 30919011410).

Notes and references

1 L. Kouchachvili, W. Yaici and E. Entchev, *J. Power Sources*, 2018, **473**, 237–248.
2 C. C. Duan, R. J. Kee, H. Y. Zhu, C. Karakaya, Y. C. Chen, S. Ricote, A. Jarry, E. J. Crumlin, D. Hook and R. Braun, *Nature*, 2018, **557**, 217–222.
3 D. Prochowicz, M. M. Tavakoli, S.-H. Turren-Cruz, K. Pandey, M. Saliba and P. Yadav, *Sustainable Energy Fuels*, 2018, **2**, 2407–2411.
4 D. Chen, Z. Lou, K. Jiang and G. Z. Shen, *Adv. Funct. Mater.*, 2018, **28**, 1805596.
5 Y. Zhou, H. J. Guo, G. C. Yan, Z. X. Wang, X. H. Li, Z. W. Yang, A. X. Zheng and J. X. Wang, *Chem. Commun.*, 2018, **54**, 3755–3758.
6 D. P. Zhao, H. Q. Liu and X. Wu, *Nano Energy*, 2019, **57**, 363–370.
7 W. H. Zuo, R. Z. Li, C. Zhou, Y. Y. Li, J. L. Xia and J. P. Liu, *Adv. Sci.*, 2017, **4**, 1600539.
8 X. Wu, Z. C. Han, X. Zheng, S. Y. Yao, X. Yang and T. Y. Zhai, *Nano Energy*, 2017, **31**, 410–417.
9 L. Fang, Y. P. Xie, Y. Y. Wang, Z. W. Zhang, P. F. Liu, N. A. Cheng, J. F. Liu, Y. C. Tu, H. B. Zhao and J. J. Zhang, *Appl. Surf. Sci.*, 2019, **464**, 479–487.
10 Y. Liu, P. F. Hu, J. R. Song, A. Umar and X. Wu, *Inorg. Chem. Front.*, 2019, **6**, 2824–2831.
11 K. S. Ashutosh and S. Debasish, *J. Mater. Chem. A*, 2017, **5**, 21715–21725.
12 W. T. Sun, L. Xiao and X. Wu, *J. Alloys Compd.*, 2019, **772**, 465–471.
13 C. Liu, W. Jiang, F. Hu, X. Wu and D. F. Xue, *Inorg. Chem. Front.*, 2018, **5**, 835–843.
14 A. K. Singh, D. Sarkar, K. Karmakar, K. Mandal and G. G. Khan, *ACS Appl. Mater. Interfaces*, 2016, **8**, 20786–20792.
15 D. P. Zhao, F. Hu, A. Umar and X. Wu, *New J. Chem.*, 2018, **42**, 7399–7406.
16 X. Wu and S. Y. Yao, *Nano Energy*, 2017, **42**, 143–150.
17 J. X. Feng, L. X. Ding, S. H. Ye, X. J. He, H. Xu, Y. X. Tong and G. R. Li, *Adv. Mater.*, 2015, **27**, 7051–7057.
18 W. Jiang, F. Hu, Q. Y. Yan and X. Wu, *Inorg. Chem. Front.*, 2017, **4**, 1642–1648.
19 Y. Zhao, M. Z. Dai, D. P. Zhao, L. Xiao, X. Wu and F. Liu, *CrystEngComm*, 2019, **21**, 3349–3355.
20 M. J. Xie, Z. C. Xu, S. Y. Duan, Z. F. Tian, Y. Zhang, K. Xiang, M. Lin, X. F. Guo and W. P. Ding, *Nano Res.*, 2018, **11**, 216–224.
21 C. Liu and X. Wu, *Mater. Res. Bull.*, 2018, **103**, 55–62.
22 L. Xing, Y. D. Dong, F. Hu, X. Wu and A. Umar, *Dalton Trans.*, 2018, **47**, 5687–5694.
23 G. M. Li, M. Z. Chen, Y. O. Yang, D. Yao, L. Lu, L. Wang, X. F. Xia, W. Lei, S. M. Chen, M. Daniel and Q. L. Hao, *Appl. Surf. Sci.*, 2019, **469**, 941–950.
24 H. F. Zhang, C. X. Lu, H. Hou, Y. Y. Ma and S. X. Yuan, *J. Alloys Compd.*, 2019, **797**, 970–977.
25 M. H. Chen, Q. X. Ge, M. L. Qi, X. Q. Liang, F. Wang and Q. G. Chen, *Surf. Coat. Technol.*, 2019, **360**, 73–77.
26 Y. Gao, S. Chen, D. Cao, G. Wang and J. Yin, *J. Power Sources*, 2010, **195**, 1757–1760.
27 Q. Yang, Z. Y. Lu, Z. Chang, W. Zhu, J. Q. Sun, J. F. Liu, X. M. Sun and X. Duan, *RSC Adv.*, 2012, **2**, 1663–1668.
28 P. H. Yang and W. J. Mai, *Nano Energy*, 2014, **8**, 274–290.
29 G. P. Xiong, P. G. He, D. N. Wang, Q. Q. Zhang, T. F. Chen and T. S. Fisher, *Adv. Funct. Mater.*, 2016, **26**, 5460–5470.
30 X. Peng, L. L. Peng, C. Z. Wu and Y. Xie, *Chem. Soc. Rev.*, 2014, **43**, 3303–3323.
31 B. T. Zhao, L. Zhang, Q. B. Zhang, D. C. Chen, Y. Cheng, X. Deng, Y. Chen, R. Murphy, X. H. Xiong, B. Song, C. P. Wong, M. S. Wang and M. L. Liu, *Adv. Energy Mater.*, 2018, **8**, 1702247–1702257.
32 F. Y. Liu, X. Chu, H. T. Zhang, B. B. Zhang, H. Su, L. Jin, Z. X. Wang, H. C. Huang and W. Q. Yang, *Electrochim. Acta*, 2018, **269**, 102–110.
33 X. H. Xiong, D. Ding, D. C. Chen, G. Waller, Y. F. Bu, Z. X. Wang and M. L. Liu, *Nano Energy*, 2015, **11**, 154–161.
34 H. Wang, H. S. Casalongue, Y. Liang and H. Dai, *J. Am. Chem. Soc.*, 2010, **132**, 7472–7477.
35 Y. Liu, D. P. Zhao, H. Q. Liu, A. Umar and X. Wu, *Chin. Chem. Lett.*, 2019, **30**, 1071–1076.
36 G. Q. Zu, J. Shen, Z. H. Zhang, B. Zhou, X. D. Wang, G. M. Wu and Y. W. Zhang, *RSC Adv.*, 2017, **7**, 10583–10591.
37 F. Y. Ning, M. F. Shao, C. L. Zhang, S. M. Xu, M. Wei and X. Duan, *Nano Energy*, 2014, **7**, 134–142.
38 G. M. Li, M. Z. Chen, Y. Ouyang, D. Yao, L. Lu, L. Wang, X. F. Xia, W. Lei, S. M. Chen, M. Daniel and Q. L. Hao, *Appl. Surf. Sci.*, 2019, **469**, 941–950.
39 P. Oliva, J. Leonardi and J. F. Laurent, *J. Power Sources*, 1982, **8**, 229–255.
40 S. H. Yang, Y. Y. Liu, Y. F. Hao, X. P. Yang, A. Goddard III William, X. L. Zhang and B. Q. Cao, *Adv. Sci.*, 2018, **5**, 1700659.

41 P. F. Hu, D. P. Zhao, H. Q. Liu, K. F. Chen and X. Wu, *CrystEngComm*, 2019, **21**, 1600–1606.
42 D. M. Xu, H. W. Wang, F. Y. Li, Z. C. Guan, R. Wang, B. B. He, Y. S. Gong and X. L. Hu, *Adv. Mater. Interfaces*, 2019, **6**, 1801506.
43 W. Quan, Y. Y. Xu, Y. T. Wang, S. C. Meng, D. L. Jiang and M. Chen, *Appl. Surf. Sci.*, 2019, **488**, 639–647.
44 H. B. Li, M. H. Yu, F. X. Wang, P. Liu, Y. Liang, J. Xiao, C. X. Wang, Y. X. Tong and G. W. Yang, *Nat. Commun.*, 2013, **4**, 1894.
45 F. F. Zhu, M. Yan, Y. Liu, H. Shen, Y. Lei and W. D. Shi, *J. Mater. Chem. A*, 2017, **5**, 22782–22789.
46 M. J. Jing, Y. C. Yang, Y. R. Zhu, H. S. Hou, Z. B. Wu and X. B. Ji, *Electrochim. Acta*, 2014, **141**, 234–240.
47 X. Wang, K. Song, R. Yang, X. Y. Jing and J. Wang, *ChemistrySelect*, 2019, **4**, 3878–3883.
48 B. Kirubasankar, P. Palanisamy, S. Arunachalam, V. Murugadoss and S. Angaiah, *Chem. Eng. J.*, 2019, **355**, 881–890.
49 T. Liu, L. Y. Zhang, W. You and J. G. Yu, *Small*, 2018, **14**, 1702407.